In Vivo Intrathecal Tracer Dispersion in Cynomolgus Monkey Validates Wide Biodistribution Along Neuraxis

Kevin Tangen, Ivan Nestorov, Ajay Verma, Jenna Sullivan, Robert W. Holt, and Andreas A. Linninger

***Abstract*—*Objective:* It is commonly believed that in intrathecal (IT) drug delivery, agent distribution is confined to a narrow region close to the injection site, thereby undermining the efficacy of the method. *Methods:* To test the claim, multimodal *in vivo* imaging was used to experimentally observe the effects of IT infusion in cynomolgus monkey, looking at cerebrospinal fluid flow, anatomy, and dispersion of a radiolabeled tracer. *Results:* At high infusion rates, the tracer reached the cervical region after only 2 h, demonstrating rapid and wide distribution. The same *in vivo* nonhuman primate imaging data also provided evidence in support of a computational fluid dynamic model for the prediction of drug distribution following IT injection. Tracer dispersion was predicted in two specimens matching the distribution acquired with positron emission tomography (PET). For the third specimen, tracer dispersion simulations were conducted as a blind study: predictions were made before *in vivo* biodistribution data was known. In all cases, the computational fluid dynamics (CFD) predictions of drug dispersion after IT administration showed close spatio-temporal agreement with tracer biodistribution *in vivo*. *Conclusion:* Validation by *in vivo* nonhuman primate data confirms our ability to predict the biodistribution of intrathecally administered agents in subject-specific models of the central nervous system from first principles. *Significance:* The experiments reinstate IT delivery as a viable administration method when targeting molecules to the whole spine or the brain. The proposed computational methodology enables rational design of novel therapies for neurological diseases that require reliable, efficient, and safe delivery of therapeutic agents to specific target sites in the central nervous system.**

***Index Terms*—Drug delivery, mathematical model, finite volume method.**

I. Introduction

INTRATHECAL (IT) drug delivery is a commonly used administration technique for anaesthesia and a number of neurological indications including, chronic pain and spasticity [1]–[6]. It is a promising modality for novel treatments such as enzyme replacement or gene therapies targeting central nervous system (CNS) diseases [7]–[9]. The capability to bypass the blood-brain barrier is often necessary to deliver molecules that would otherwise be restricted from reaching their intended target in the CNS [10]. Prior studies [11] seem to suggest that IT injection administers the drug only to a very narrow region close to the injection site. However, experimental and theoretical work by our group [12]–[14] show that with proper infusion settings, IT injection can achieve wider dispersion than has been reported previously. The important difference between prior studies and the study presented here is that the selection of optimal infusion parameters for the desired biodistribution within the central nervous system requires quantitative methods [15]–[18]. Choosing optimal infusion settings is neither intuitive, nor can be done by trial-and-error animal experimentation due to the large number of variables and high cost. Rather, selection of optimal parameters requires a means by which to *predict* biodistribution of intrathecally administered therapeutics prior to conducting trials for new treatments. The ability to predict drug spread is highly relevant for designing infusion protocols for targeting drugs to points distal to the injection site, especially the brain. Computational models offer a rational framework to predict biodistribution of intrathecally (IT) infused agents. Prior work with human CNS surrogates and healthy imaging subjects has demonstrated the ability to simulate cerebrospinal fluid (CSF) flow patterns [12], [13], [19] and biodistribution of intrathecally administered agents [14] using established computational fluid dynamics (CFD) techniques. However, since it is infeasible to acquire in vivo human data solely for the purpose of validating simulated tracer spread, a nonhuman primate (NHP) model was chosen for its close approximation to the human central nervous system. Moreover, an animal model with anatomy similar to human allows more reliable translation of interspecies assumptions when transitioning CFD predictions of IT drug administration from animal to human studies. While invasive experiments for model validation on human subjects were considered, they were dismissed due to risks associated with radiolabeled tracers as well as the invasiveness of the procedures in a highly

Manuscript received December 21, 2018; revised June 21, 2019; accepted July 7, 2019. Date of publication July 23, 2019; date of current version March 19, 2020. This work was supported by Biogen and the National Science Foundation CBET-1301198. *(Corresponding author: Andreas A. Linninger.)*

K. Tangen is with the Department of Bioengineering, University of Illinois at Chicago.

I. Nestorov and A. Verma are with Biogen Inc.

J. Sullivan and R. W. Holt are with Invicro LLC.

A. A. Linninger is with the Department of Bioengineering, University of Illinois at Chicago, Chicago, IL 60607 USA (e-mail: linninge@uic.edu).

This paper has supplementary downloadable material available at http://ieeexplore.ieee.org, provided by the authors.

Digital Object Identifier 10.1109/TBME.2019.2930451

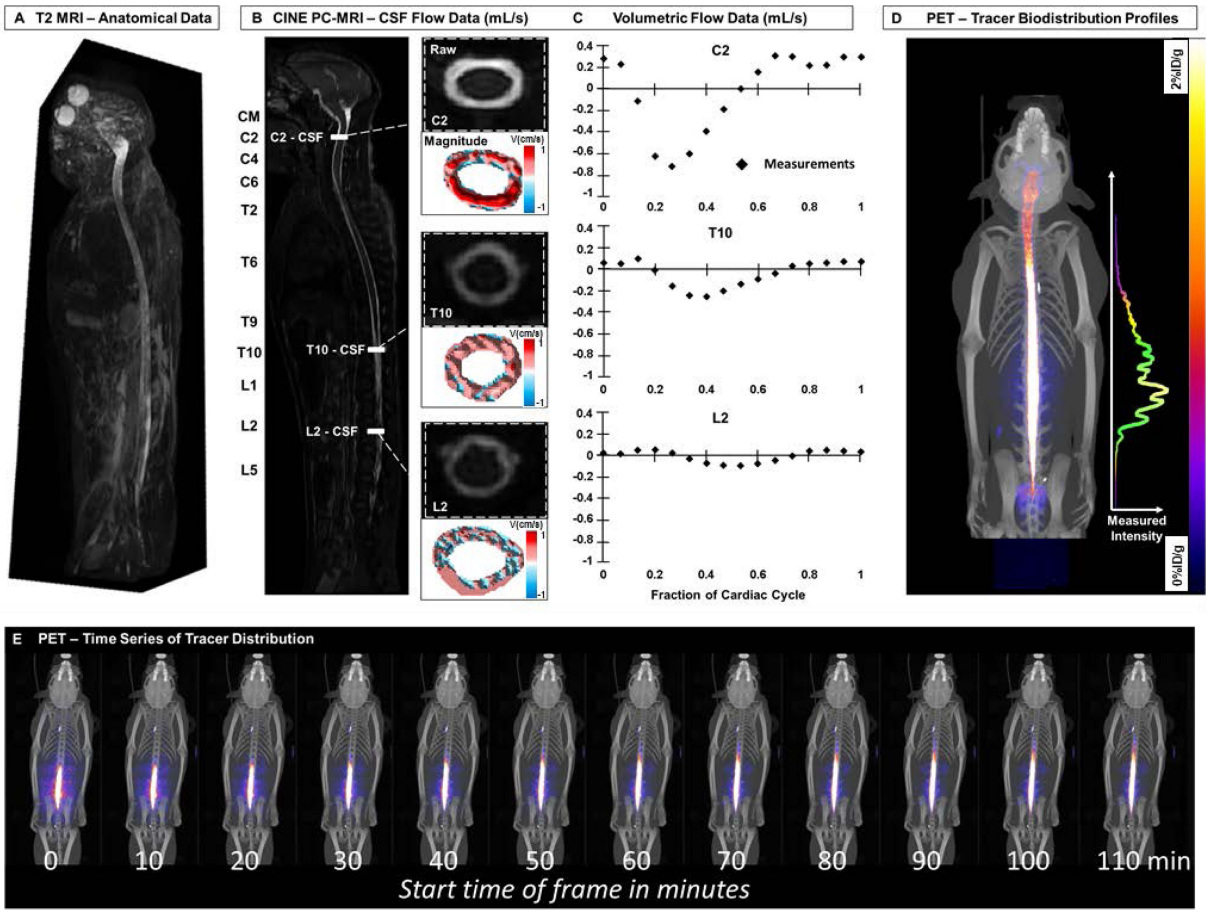

Fig. 1. Overview of the multi-modal experimental design to validate tracer distribution after IT injection in Cynomolgus monkey. (A) T2 MRI data is acquired for cranial and spinal CSF-filled spaces, seen here as a 3D image set for specimen-3. Subject-specific anatomical dimensions from each monkey are used to generate an anatomically consistent computational mesh. (B) MRI Cine phase-contrast CSF velocity measurements are acquired at axial planes, represented as white overlays indicate the anatomical position of the three regions of interest (C2, T10, L2). The raw axial image displays the CSF in white, which forms an annulus around the spinal cord, in black. A CSF velocity contour map is extracted for each plane, visualized here at peak systole (~0.3 of cardiac cycle). Red represents flow velocity in the caudal direction and blue is cranial flow. Color scale is consistent for all three axial sections in C2, T10, L2. It can be noted that the velocity magnitude is greatest in the cervical region, which is confirmed by the plot in panel C. (C) CSF velocity measurements from the three axial planes are plotted, black diamonds, over a full cardiac cycle. (D) PET data were acquired continuously for 120 minutes following IT injection of tracer into the lumbar CSF space. Drug concentration profiles are extracted with VivoQuant (InviCRO, Boston, MA) and average concentrations are plotted along the neuraxis. (E) Time series images show distribution of radiolabeled tracer from 0–120 minute post-lumbar injection in Monkey-3. PET image intensity overlaid on CT anatomical image data of monkey subject. PET is shown in fire color scale, CT is shown in gray scale. PET images are scaled from 0–2% ID/g (percentage injected dose per gram tissue).

sensitive area of the human. The cynomolgus monkey provided a safe and informative platform for acute IT infusion study. It validated subject-specific predictions of tracer spread against non-invasive *in vivo* positron emission tomography (PET) measurements as the gold standard.

II. Materials and Methods

The image processing and segmentation workflow to produce detailed models of biodistribution for IT administered agents in the CSF is composed of three main phases; (i) data acquisition, (ii) subject-specific model generation, and (iii) CFD simulation of subject-specific CSF flow and tracer biodistribution. A large number of dynamic experimental observations spatially distributed along the neuraxis were collected to build the CFD model. Using magnetic resonance imaging (MRI), anatomical information as well as subject-specific CSF flow measurements were acquired for the cervical, thoracic and lumbar regions. PET imaging was used to track tracer concentration profiles along the entire neuraxis for up to two hours after intrathecal injection. The collection of anatomical, CSF flow and tracer dispersion data are summarized in Figure 1 for monkey-3, (images for monkey-1 and monkey-2 are similar, but are omitted due to space limitations). *Animal Care.* Healthy 3–4 year old Cynomolgus monkeys (Covance China and Covance Vietnam), with weight 3–4.3 kg, were housed in dedicated non-human primate facilities at MPI Research (Mattawan, MI, USA). Animals were housed in primate pair housing caging. Following tracer administration, animals were individually housed until radioactive decay was complete (at least 10 half-lives; 127 hours). While individually housed, animals had companion study animals housed in the same room for visual enrichment. Additional animal enrichment was provided. Fluorescent lighting was provided via an automatic timer for approximately 12 hours per

TABLE I
INFUSION PARAMETERS AND BIOMETRICS OF CSF SPACES FOR MONKEY SPECIMEN M-1, M-2, M-3

	M-1	M-2	M-3	Mean
Biometrics				
CSF Volume (mL)	17.46	12.35	13.24	14.35
Length spine (cm)	34.62	30.78	30.97	32.12
Stroke Vol. (mL)	0.126	0.032	0.058	0.072
Heart rate (bpm)	112	119	119	117
Infusion Settings				
Injection Vol (mL)	1.8	1.8	0.36	-
INJ:CSF Ratio %	10.31	14.57	2.72	-
Inj. Duration (min)	2	1	1	-
Tracer				
Conc. (mol/mL)	$9.27*10^{-8}$	$1.42*10^{-7}$	$2.23*10^{-7}$	-
Amount (mol)	$1.67*10^{-7}$	$2.56*10^{-7}$	$8.01*10^{-8}$	-

day. Tap water was supplied ad libitum via an automatic water system. Animals received an adequate supply of primate chow except during designated fasting periods. Animal welfare for this study was in compliance with the U.S. Department of Agriculture's Animal Welfare Act (9 CFR Parts 1, 2, and 3). Guide for the Care and Use of Laboratory Animals, Institute of Laboratory Animal Resources, National Academy Press, Washington, D.C., 2011, was followed. All study procedures were reviewed and approved by the Institutional Animal Care and Use Committee at MPI Research prior to the start of the study. Each animal was fasted for a minimum of 4 hours prior to induction of anesthesia with ketamine (10–25 mg/kg. IM). Following anesthetization, animals were placed on isoflurane (1–2%) with oxygen (2%) for the lumbar puncture and imaging. Vital signs were monitored throughout the procedure. Lactated Ringer's Solution was administered in a 5 mL subcutaneous (SC) bolus both pre- and post-imaging. Each animal was also given Metacam (0.2 mg/kg, IM) and Ceftiofur (2.2 mg/kg, IM, SID).

A. Primate Intrathecal Infusions

Approximately 500 μCi of ^{64}Cu-DOTA was injected intrathecally by an experienced surgeon using a 22-gauge spinal needle introduced in the L3/L4 intrathecal space using aseptic technique. Animals were injected intrathecally with 0.36 mL or 1.8 mL of ^{64}Cu-DOTA (formulated in aCSF), over a duration of 1-2 min with an infusion pump. The experimental scenario information is tabulated for each monkey specimen in Table I.

B. PET and MRI Image Acquisition

Subject-specific anatomical information was acquired by T2 MRI. All animals were imaged on a 1.5T Siemens Symphony MRI scanner (Siemens Medical Systems, Erlangen, Germany). High-resolution MRI of the spine and cranium were acquired in separate acquisitions within a single imaging session while each animal was under anesthesia. Images were acquired in axial orientation using a 3D T2 fast-spin echo (FSE) sequence with one excitation. Cranium data were acquired with a clinical CP extremity coil, voxel size of $0.7 \times 0.7 \times 2$ mm, acquisition time of 8.05 min, TR of 12.5 ms, and TE of 6.25 ms. Body data were acquired with a clinical body coil, voxel size of $0.35 \times 0.35 \times 2$ mm, acquisition time of 13.97 min, TR of 11.82 ms, and TE of 5.91 ms.

C. CSF Flow

CSF flow velocity was acquired in a separate imaging session using a 1.5T Philips Intera MRI scanner (Philips Healthcare, Andover, MA, USA). High resolution images of the cranium and spine were collected using a 2D phase contrast CINE MRI using ECG for cardiac gating. Initial image acquisition was obtained with a standard 2DPCA CINE CSF flow sequence in sagittal and axial planes along with appropriate localizer sequences using VCG leads to allow for cardiac gating in the sagittal/axial plane. Cranium and cervical spine data were acquired with a SENSE 6-channel head coil or SENSE Flex-M coil, and spine data were acquired with an R1 linear linear surface coil. Detailed settings for the cranial flow measurements are given in Supplement-I.

D. PET/CT

^{64}Cu-DOTA tracer biodistribution data were acquired using PET imaging (Focus220 microPET, Siemens Medical Systems, Knoxville, TN). Dynamic whole-body continuous bed motion PET data were acquired for 0-120 min in 3D list-mode and re-binned into 2D sinograms. PET images were reconstructed by a 2D Ordered Subset Expectation Maximization (OSEM2D) algorithm with 14 subsets and 4 iterations. Corrections were made for detector normalization, decay, dead-time, randoms, and attenuation into images with $256 \times 256 \times 693$ pixels and $0.95 \times 0.95 \times 0.80$ mm voxels. After each PET scan, a CT (CereTom CT, NeuroLogica Corp, Danvers, MA) was acquired for anatomical registration. All animals were imaged on a specially designed bed, which was transferred from the PET to the CT to allow consistent positioning of the animal between the two modalities. CT acquisition time was 6 minutes and based on an axial range of 450 mm, an energy window of 120 kVp, with 720 projections per rotation, and 4 seconds per projection.

PET and MRI data were not acquired concurrently. PET and CT, T2 MRI, and phase contrast MRI scans were collected separately for each animal. Animal positioning was not intentionally maintained between scans (with the exception of PET and CT scans). PET and CT, T2 MRI, and phase contrast MRI scans were analyzed independently of each other. Immediately after each PET scan, a CT scan was acquired for attenuation correction and to support analysis of the PET data. Animals were imaged on a specially designed bed, which was transferred from the PET to the CT to allow consistent positioning of the animal between the two modalities. These acquisition details have been clarified in the methods of the manuscript. All image data were collected within a 6-month period as animals and scanners were available.

E. PET Acquisition of Tracer Concentration Profiles Along the Neuraxis

Subject-specific anatomical information was acquired by T2 MRI in axial, coronal, and sagittal views using a Philips

Intera 1.5T MRI (Philips Healthcare). Image resolution in all specimen ranged from 0.25 × 0.25 mm to 0.7 × 0.7 mm in the axial plane and 0.9 × 0.9 mm in the sagittal plane. CSF flow velocity was acquired at axial planes (e.g., C4, T6, L4) by phase-contrast MRI. The CSF flow field was reconstructed with methods described previously [11]. Additionally, tracer biodistribution data was acquired using PET imaging (Focus220 microPet, Siemens Medical Systems, Knoxville, TN). Dynamic listmode PET data were acquired from 0-120 minutes post-IT injection and reconstructed into 12 × 10 min frames.

F. Analysis of PET Data Along the Neuraxis

The cranial and spinal CSF space was segmented based on T2-weighted MRI intensity and manually edited by an expert. Each reconstructed dynamic PET scan was corrected for any between-frame motion and co-registered to CT. ^{64}Cu-DOTA concentration in the spinal column was extracted from volumes-of-interest (VOIs) defined by applying a combination of manual and automated segmentation thresholds to the CT. Spinal column VOIs include ^{64}Cu-DOTA signal from both the spinal cord and CSF within the intrathecal space.

The transverse center of the spine was calculated for each axial slice of the spinal column segmentation. The spine was then parameterized by approximating the distribution of these points using a seventh degree polynomial. To condense the spine to a one-dimensional representation along the neuraxis, this parameterization was discretized into 1 mm sections starting from the cisterna magna and moving in the inferior direction. For each segment, a rectangular prism of 1 mm thickness was oriented perpendicular to the spinal parameterization at that point. The sum of the PET signal in that prism was calculated and reported as the tracer concentration profile along the spine using VivoQuant (InviCRO, Boston, MA).

G. Subject-Specific Model Generation

Geometry information and monkey biometrics acquired from imaging data were extracted and used as input for reconstructing a subject-specific computational mesh of the spinal and cranial CSF filled spaces. An overview of the MR and PET data acquisition is given in Figure 1. The monkey CFD meshes (n = 3) were generated in ITK-Snap using semi-automated and manual segmentation methods. Mesh generation tool ANSYS ICEM (Canonsburg, PA) was used to construct a volumetric mesh for each individual monkey, including microanatomical features such as nerve roots. Mesh density was varied between 10,000–40,000 cells/ml. Approximately 30,000 cells/ml yielded mesh independent results performed with the same procedures described for human IT drug delivery settings in a series of papers [19], [20], [12]–[14]. The integration stepsize was chosen between dt = 1.10^{-3}–5.10^{-2} s; a value of dt = 1.10^{-2} was used in the results reported in the figures. A pressure-based solver with fixed time stepping, and incompressible fluid was selected in the simulations.

The computational fluid domain was established by inserting a CAD mesh for the injection needle into the intrathecal space of the anatomical mesh of the spinal subarachnoid spaces. After remeshing, the combined computational domain encompassed the infusion catheter for dynamic drug dispersion simulations as shown in Figure 2B. Mesh quality was locally improved especially near the insertion catheter and nerve roots by ICEM smoothing features until the maximal face skewness was below 0.95 and minimal orthogonal quality was above 0.1.

H. Reconstructing Wall Deformation to Drive CSF Flow

It is our hypothesis that the oscillatory CSF fluid displacement from the cranial and the spinal compartment observed in MRI is equal to the total volumetric expansion or contraction of the spinal CSF filled space. This proposition is consistent with the Monro-Kellie doctrine [12] and mass conservation. Moreover, amplitude attenuation of the stroke volume at three regions of interest (cervical, thoracic and lumbar) observed in MRI support the proposition of gradual spinal CSF volume deformation along the neuraxis. The continuity equation (1) for a fluid flowing in a deformable domain correlates amplitude changes of the volumetric CSF flow rate to spinal deformations along the neuraxis. This reasoning enables inference of spinal deformations, which are very small so that they cannot be directly observed with MRI. However, even small deformations are necessary to accommodate CSF exchange between cranial and spinal compartments in closed models of the CNS [12]. The computed deformations were used to induce pulsatile CSF motion whose waveform of the CSF flow velocities matched experiments as described in previous work [13]. In brief, we start from the continuity equation (1), which relates the volumetric CSF flow rate, $Q(x,t)$, to the cross-sectional area of the spinal subarachnoid space, where $A(x,t)$ denotes the cross-sectional area at an axial location x along the neuraxis.

$$\frac{\partial A\,(x,t)}{\partial t} + \frac{\partial Q\,(x,t)}{\partial x} = 0 \tag{1}$$

At the cervical region, CSF flow enters the spinal subarachnoid space in systole. The total volumetric CSF inflow rate in each period is accommodated by a corresponding volumetric expansion of the dura along the neuraxis. We encoded the temporal profile of the volumetric flow rate measured in the cervical, thoracic and lumbar region as a Fourier series. To obtain a continuous function along the neuraxis, $Q(x,t)$, we used linear finite element interpolation as described in [13]. The interpolation formulae with Fourier coefficients for monkey-1 are listed in supplement-II. After differentiation in space and integration in time, cross sectional area deformation, $A(x,t)$, for each point x along the neuraxis and time point t can computed as in eq. (2).

$$A\,(x,t) = A_0\,(x) - \int_0^t \frac{\partial Q\,(x,\tau)}{\partial x} d\tau \tag{2}$$

The information for the undeformed cross sectional area, $A_0(x)$, is extracted from anatomical MRI data. The Fourier-finite element formulation is convenient for volumetric flow information. The percent area change reported in II was computed with eq. (3). The cross sectional area deformation is enforced

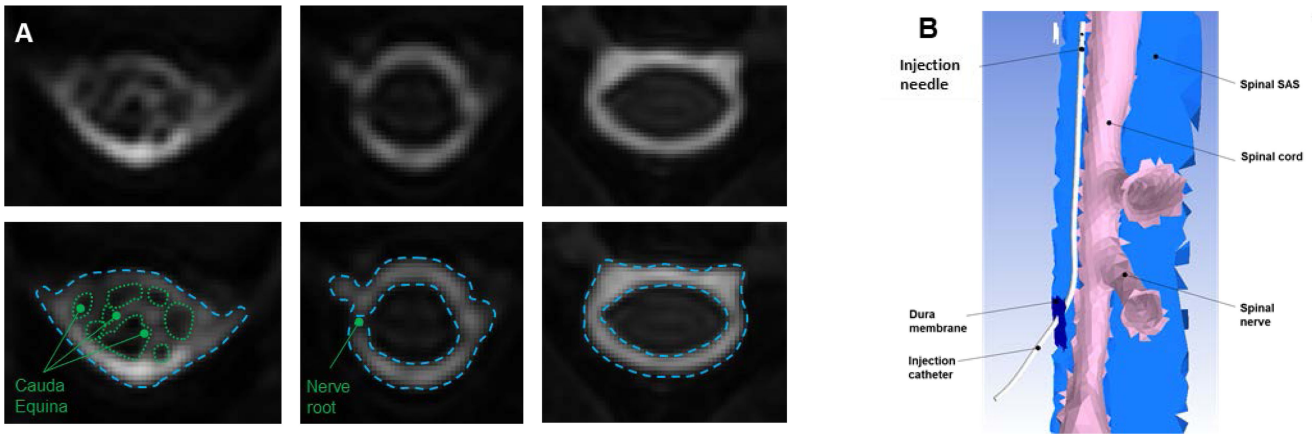

Fig. 2. Microanatomical features resolved in axial cross sections of the spinal SAS in specimen monkey-1. MRI image data of cross sectional areas are similar in all three monkey specimens (data for monkeys not shown). (A) The raw MRI images (top row) visualize the cauda equina or nerve bundles in the lumbar and sacral spine branch through the spinal SAS. Nerve roots project laterally from the spinal cord across the CSF through the outer dura membrane. The ventral and dorsal aspects of the spinal SAS are also delineated with dashed lines. Illustration of spinal CSF space reconstruction are depicted in bottom row, using blue dashed lines to delineate the inner (pia mater) and outer (dura mater) membranes of the CSF space. Green dotted lines show the nerve root and cauda equina boundaries. (B) In addition to the anatomical spaces, a computational mesh for the injection needle was generated. The needle mesh was inserted into the subject-specific monkey mesh at the injection point. The interior elements of the combined meshes were remeshed for the IT tracer infusion simulation.

TABLE II
COMPUTATIONAL PREDICTIONS OF CSF FLOW FIELD, STROKE VOLUMES, VOLUME CHANGES, AND SPINAL AREA DEFORMATIONS

	Parameter	Units	M1	M2	M3	Mean
Cervical (C2)	Stroke vol	mL	0.126	0.032	0.058	0.072
	Peak Sys	mL/s	-0.766	-0.299	-0.419	-0.495
	Peak Dia	mL/s	0.309	0.084	0.176	0.190
Thoracic (T8-T10)	Stroke vol	mL	0.038	0.011	0.019	0.023
	Peak Sys	mL/s	-0.249	-0.165	-0.140	-0.185
	Peak Dia	mL/s	0.114	0.036	0.075	0.075
Lumbar (L2)	Stroke vol	mL	0.018	0.005	0.007	0.010
	Peak Sys	mL/s	-0.093	-0.092	-0.040	-0.075
	Peak Dia	mL/s	0.054	0.054	0.036	0.048
Volume Change	Volume	mL	17.46	12.35	13.24	14.35
	Max Vol	mL	17.58	12.38	13.29	14.42
	% change	%	0.72	0.26	0.44	0.48
Area Change	Norm A	m^2	0.228	0.158	0.175	0.187
	Max A	m^2	0.235	0.162	0.180	0.193
	% change	%	3.31	2.27	2.89	2.83

Stoke vol-stroke volume, Peak Sys- peak systolic velocity, cranio-caudal flow; Peak Dia – peak diastolic velocity, caudocranial flow.

as explicit wall displacements in simulations as described next.

$$area\ change\,[\%] = \frac{A\,(x,t) - A_0\,(x)}{A_0\,(x)}\ x\ 100\,[\%] \qquad (3)$$

I. CFD Simulation in Deformable Spinal Compartment

Cerebrospinal fluid flow simulations were conducted in ANSYS Fluent using techniques whose entire scope cannot be reiterated here, but more details on image processing to preserve anatomical features, segmentation to generate tetrahedral volume meshes as well the procedures to set up and ensure mesh independent results are described elsewhere [12]–[14]. A brief summary follows: Spinal dura deformations were implemented with moving fluid domain using moving wall boundary conditions in ANSYS Fluent. Pulsatile CSF flow inside the closed spinal subarachnoid space was implemented as an explicit boundary movement with remeshing of the fluid domain in each time step. To impose the area deformations computed with eq. (2), the positional coordinate of each boundary point was moved in a direction perpendicular to the average face normal. All boundary points (= dura surface in the subarachnoid space) located at given spinal level x were subjected to the same displacements. This was achieved by grouping surfaces for the brain parenchyma and the outer border of the spinal CSF space (spinal dura) into specific wall boundary types with ICEM ANSYS Fluent. *User Defined Functions* (UDF) programmed in the C language encoded uniform wall displacements for each group at each time step along the surface normal. The integral of the area change imposed by surface node displacements corresponded to changes in CSF stroke volume amplitude according to eq. (2). The CSF flow field $\vec{u}(x,t)$ were thus computed by solving the Navier-Stokes equations with a moving boundary approach in ANSYS Fluent.

J. CSF Mediated Species Transport

Convection and diffusion of a tracer in the CSF is governed by eq. (4). The integral of the across velocity vectors, $\vec{u}(x,t)$, at given cross section is related to volumetric flow rate, $Q(x,t)$, as in eq. (5). In our numerical approach, it is obtained by summing the velocity information from MRI for each pixel of a cross sectional area. In direct numerical simulation, transport could occur to bulk convection or by micro-mixing. We showed previously that micro-mixing eddies and vortices induced by oscillatory CSF flow around micro-anatomical features in the spinal subarachnoid space are able to cause rapid tracer dispersion, even in the absence of net bulk flux. Actually since the CSF domain (= cranial and spinal CSF spaces) is closed in our proposed CFD simulation approach, the net flux,

$Q_{net}(x)$, at a cross sectional location x along the neuroaxis is zero over one cardiac cycle, R, as in eq. (6). The effect of micro-mixing induced tracers dispersion from the injection site in caudocranial direction was also demonstrated previously in human simulations with closed cranial and spinal CSF compartments [12], [14]. Accordingly, micro-mixing phenomena, not bulk flow, convey tracers from the injection site in caudocranial direction.

$$\frac{\partial C}{\partial t} + \vec{u}\,(x,t) \cdot \vec{\nabla} C\,(x,t) = \vec{\nabla} \cdot \left[D_{CSF} \vec{\nabla} C\,(x,t) \right] \quad (4)$$

$$Q\,(x,t) = \oint \vec{u}\,(x,t)\; dA\,(x,t) \quad (5)$$

$$Q_{net}\,(x) = \int_0^R \frac{\partial Q\,(x,t)}{\partial x} dt = 0 \quad (6)$$

K. CSF Generation, Absorption and Molecular Diffusion

We showed in prior studies that bulk CSF production had a negligible contribution to tracer transport and was accordingly omitted in the monkey simulations. Furthermore, parametric studies with diffusivities varying over several order of magnitudes further showed that the diffusion contribution in spinal intrathecal administration settings was small compared to rapid geometry induced mixing [12]. Accordingly, the molecular diffusivity, D_{CSF}, of the tracer was set to zero in the simulations.

Intrathecal tracer infusion predictions used the experimental infusion parameters for each monkey as input as listed in Table II. Biodistribution using a convective species transport equation was predicted for a period of 120 minutes post-infusion. Predicted spatiotemporal tracer biodistribution profiles were plotted at ten minute intervals from t = 0 to t = 110 minutes, for comparison to *in vivo* PET data. Tracer dispersion was predicted without the need for further adjustable parameters in two specimens. For the third specimen tracer dispersion simulations were conducted as a blinded study, in which predictions were made before biodistribution was known to the modeling group**.** Quantitative analysis consisted of comparison of tracer front position and tracer spread rates between the experimental data and the computed tracer concentration profiles.

III. Results

A. Biometrics and CSF Flow Data Results

The set of image acquisition data for monkey-3 is summarized in Figure 1. Anatomical MR data covered the entire cranial and spinal subarachnoid space (SAS) is shown in Figure 1A for subject-specific analysis of the CSF volumes and dimensions. Figure 1B depicts the axial CSF velocity data, and extracted CSF flow profiles are plotted in Figure 1C. CSF stroke volumes and volume of cranial subarachnoid spaces for three monkey subjects are tabulated in Table II. The PET data for intrathecally administered tracer concentration along the entire neuraxis are shown in Figure 1D–E, for the initial time point ten minutes after the injection (T = 0 min) until two hours after injection (T = 110 min).

B. Subject-Specific Image Reconstruction

The computational meshes, shown for monkey-1 in Figure 3A, encompasses the cranial SAS, cerebral ventricles, spinal SAS, and the brain and spinal tissue volumes. We also reconstructed microanatomical features up to the limit of MRI resolution, such as nerve roots as shown in Figure 3A. This microanatomical feature detail interrupts the annular cross sections of CSF flow in the spinal subarachnoid spaces. It critically affects the micromixing patterns thus leading to geometry induced flow with chaotic advection, which is responsible for the rapid drug action of anesthetics observed clinically [21]. The effect of micromixing on drug dispersion was quantified previously for human subject-specific simulations in our group [12], [13].

C. Inference of Spinal Compliance and Deformation From MRI Velocity Measurements

Our *geometry induced micro-mixing* hypothesis suggests that CSF displacement from the cranial to the spinal subarachnoid space (= stroke volume) brings about an equal volume displacement of the spinal subarachnoid space. The gradual attenuation of the stroke volume from the cervical to the thoracic and the lumbar region is evidence in support of the deformation hypothesis. Flow waveforms for each animal subject were derived from the fluid velocity data acquired by axial MRI. We solved eq. (1) in space and time by using a finite element Fourier approximation of $Q(x,t)$ to obtain the spectral values for $A(x,t)$. The resulting cross sectional deformation of the spinal subarachnoid space $A(x,t)$ is plotted in Figure 4. Complete maps of percent cross sectional area changes for the spinal deformation in three monkeys are depicted in Figure 4A. We hypothesize that pulsatile CSF motion with geometry induced eddies served as the driving force for caudocranial drug dispersion.

D. Computational Predictions of CSF Flow Dynamics

Dynamic 3D CFD simulation with moving dura boundary conditions predicted the CSF flow field in the spinal and cranial subarachnoid space. The periodically pulsatile CSF flow field was computed as a function of the experimentally observed CSF stroke volumes in the compliant spinal compartment. Simulated predictions of CSF flow field velocity, volume change, and area deformation are tabulated in tables of Supplement II. Microanatomical features, especially nerve roots, impact the CSF flow field generating chaotic advection (also described as geometry induced mixing) which manifests as recirculation eddies in Figure 3B.

Initially, drug dispersion was dominated by the infusion impulse. After 2 minutes when infusion ceased, CSF dispersion was mainly driven by natural CSF pulsations. The computed CSF flow fields match the measured velocity data closely at all three areas of interest (C2, T10 and L2) with an $R^2 = 0.96$ for all spatiotemporal concentration data. Figure 3C depicts raw images, measured and predicted flow fields, and the reconstructed anatomical CSF domain for three monkey specimen. CSF flow field computations have the advantage that they do not merely match the measured CSF flow fields at regions of interest, but

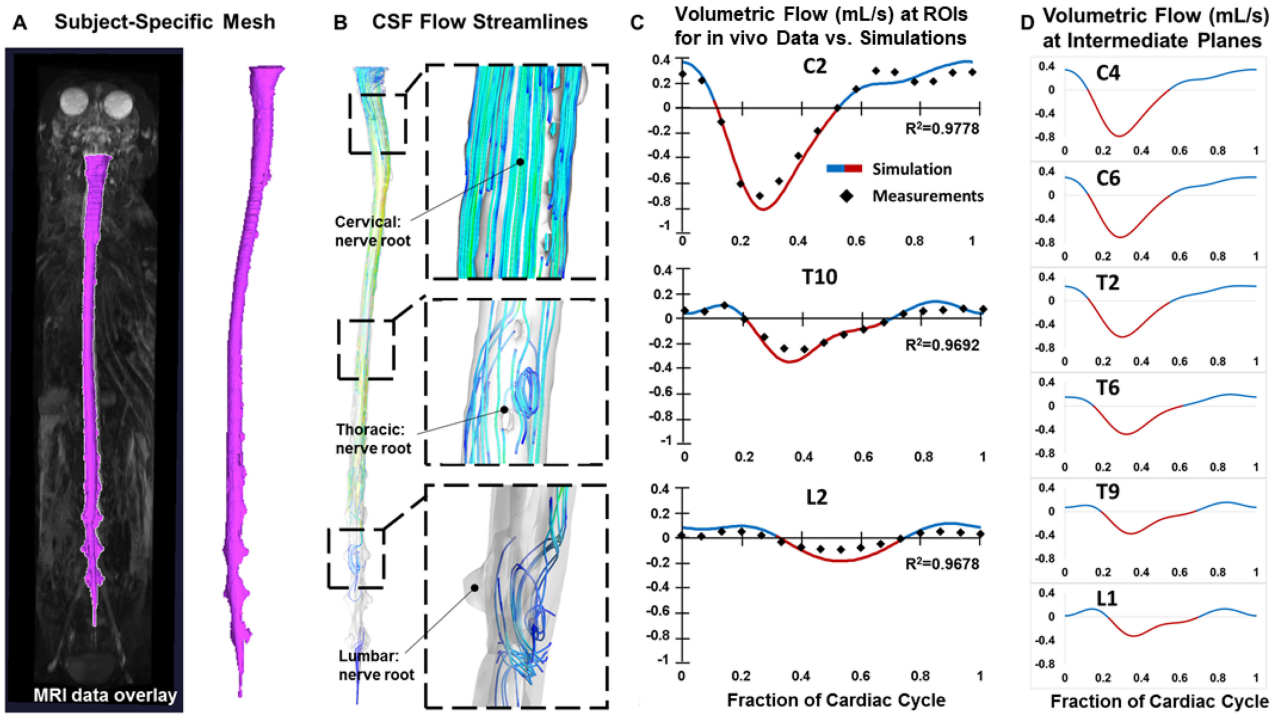

Fig. 3. Subject-specific reconstruction of the anatomy of the spinal compartment and CSF flow field in Monkey-1. (A) Subject-specific anatomical dimensions from monkey specimens are used to generate a detailed subject-specific computational mesh including microanatomical features (nerve roots). Flow simulations and tracer distribution are carried out in ANSYS Fluent. (B) Predicted CSF profiles are visualized by velocity streamlines in the cervical, thoracic, and lumbar spinal regions. Flow fields adjacent to nerve roots exhibit chaotic advection due to geometry-induced mixing. (C) Comparison of CSF flow simulations with CSF velocity measurements along the neuraxis (cervical - C2, thoracic - T10, lumbar - L2). There is close agreement at all three planes with an $R^2 > 0.96$ (Color coding of flow rates in mL/s, red indicates flow in caudal, blue in cranial direction). (D) Predicted CSF flow field in intermediate planes along the neuraxis. CSF flow field computations have the advantage that they provide detailed CSF velocity vectors in every point in time and space of the neuraxis.

that they also provide detailed CSF velocity vectors in every point in time and space of the neuraxis, as shown in Figure 3D. Therefore, a complete flow map of CSF flows in the spinal subarachnoid space even outside the three areas of interest can be generated. Flows and inferred deformations are displayed in Fig. 4. Furthermore, we have encoded the CSF stroke volumes, the inferred area deformations, and the dynamic pressure changes using a finite element Fourier approximation so that readers can extract the information for each point in space in time (see Supplement I).

E. Tracer Biodistribution Profile Extraction and Comparison

Predicted tracer dispersion after bolus infusion for all three monkey experiments is shown in Figure 5. The simulated tracer dispersion front expanded both cranially and caudally, with a more rapid spread of the tracer front in the cranial direction. The center of mass remains close to the lumbar injection site. Tracer front spread reached the cisterna magna level of the spinal cord after 120 minutes for subject-1. In subject-3, tracer spread is more confined to the site of injection. The experimental data and simulation results predicted using subject-specific and monkey anatomy are in good agreement for all three monkey trials. All predicted tracer spread profiles in Figure 5 demonstrate that the tracer disperses both cranially and caudally. However, the tracer profile dispersed faster from the infusion site towards the cranium. Also, the center of mass remains stationary slightly above the injection site. It should be noted that tracer distribution in Monkey-1 and Monkey-2 exhibited a faster and wider biodistribution than Monkey-3. It is plausible that these differences occur due to the larger infusion volume. At higher infusion rates (1.8 mL, 10–15% of specimen CSF volume) the injected agent reached the cranial space in two hours. With a low infusion rate (0.36 mL, ∼3% (2.72%) specimen CSF volume), the tracer remained relatively more confined to the infusion site.

Figure 6 compares tracer concentration profiles at the beginning of the infusion and after two hours of CSF induces tracer spread. Visual inspection confirms that the predicted profiles are in reasonable agreement with experimental observations.

The deformable spinal domain using a moving boundaries in ANSYS Fluent entailed remeshing of the fluid domain in each time step. This is computationally very expensive, putting a limit the time stepping as well as on mesh size. The simulation results in Figs. 3 and 5 were obtained with a stepsize of $dt = 0.01$s and a mesh density of 30,000 tetrahedral cells per ml. It should be emphasized that the fluid domain in our CNS-wide flow and species transport simulations is closed so that the CSF pulsates in its position along the neuraxis, but the total amount remains constant. Thus, net bulk CSF exchange between the

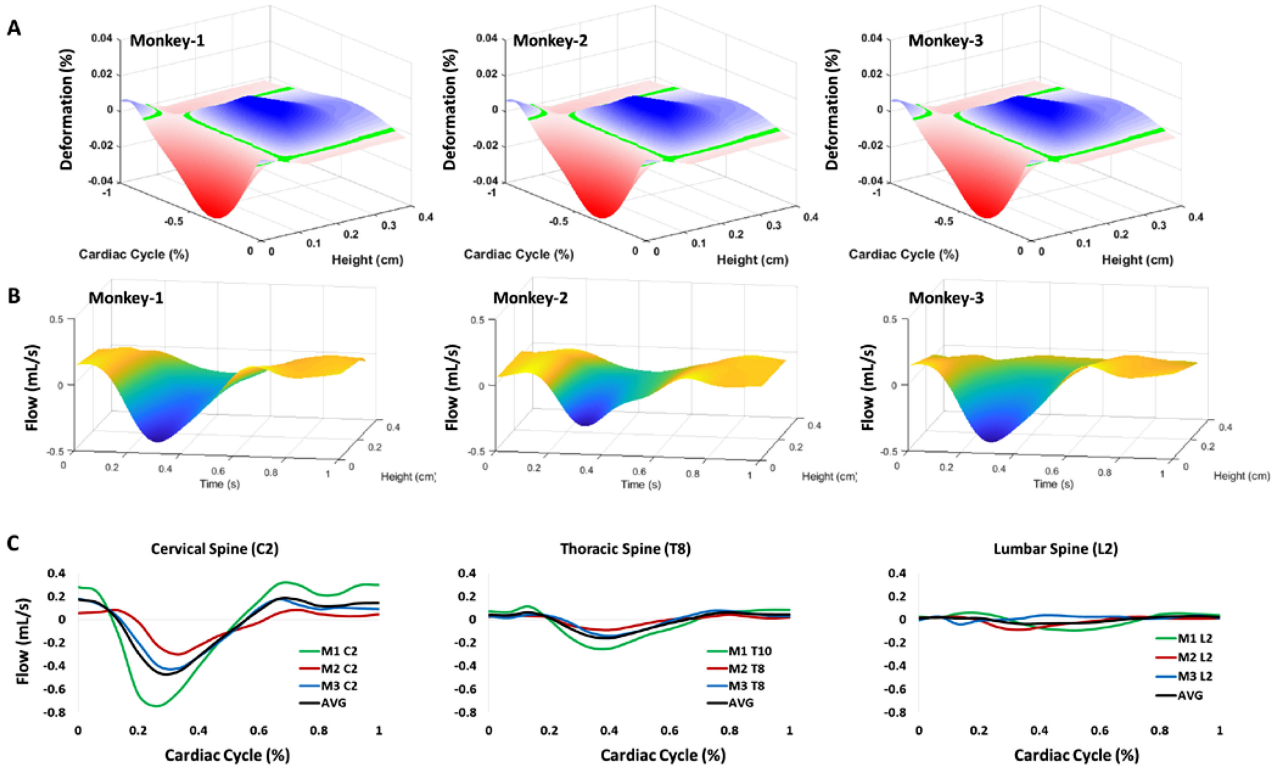

Fig. 4. Inference of spinal deformation (fluid-structure interaction) from *in vivo* CSF flow measurements. (A) The area deformation and displacement of the spinal subarachnoid space (compliant dura compartment) was inferred from the *in vivo* measured attenuation of the CSF stroke volume along the neuraxis and the help of equation 1. The resulting area change (%) for monkey-1, 2, and 3 are depicted. (B) The best fit volumetric flow map is given for the complete space and time in the spine over a cardiac cycle (Fourier finite element encodings of the volumetric flow, area deformation, and oscillatory pressure maps are given in tables of Supplement I). This pulsatile CSF motion serves as the driving force of drug distribution. (C) Volumetric flows are plotted to compare the magnitude and waveforms between monkey specimens at the cervical, thoracic, and lumbar regions.

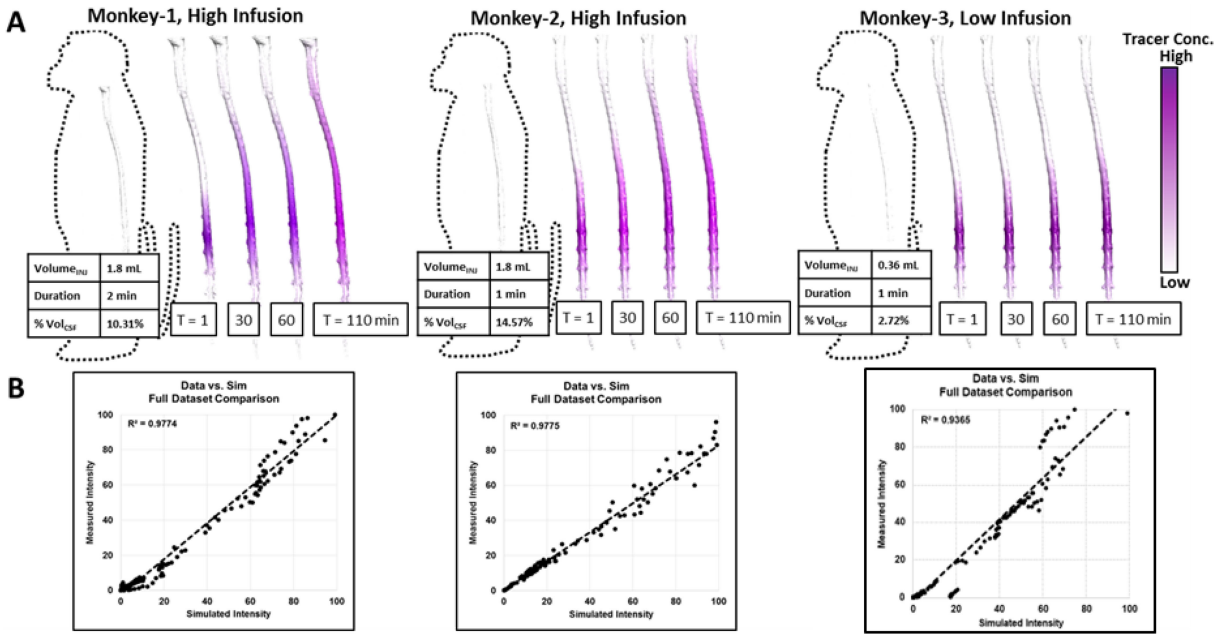

Fig. 5. Statistical analysis of simulated and experimental results of IT administered tracer spread. (A) Simulated advancement of the tracer concentration profiles in monkey specimens over the course of two hours after injection. Tracer concentration profiles are visualzed in purple along the neuraxis for different time points (T = 1, 30, 60, 110 min). Biodistribution in Monkey-1 and Monkey-2 spreads cranially and reaches the top of the spinal CSF after two hours. Because of the lower infusion flow rate, biodistribution in Monkey-3 remained closer to the injection site extending to the thoracic spinal level. The dispersion pattern exhibited a cranial bias for all monkey specimens. (B) Comparison of simulated tracer concentration with measured tracer concentration data shows good agreement in the temporal and spatial dimensions ($R^2 = 0.97, 0.97, 0.93$).

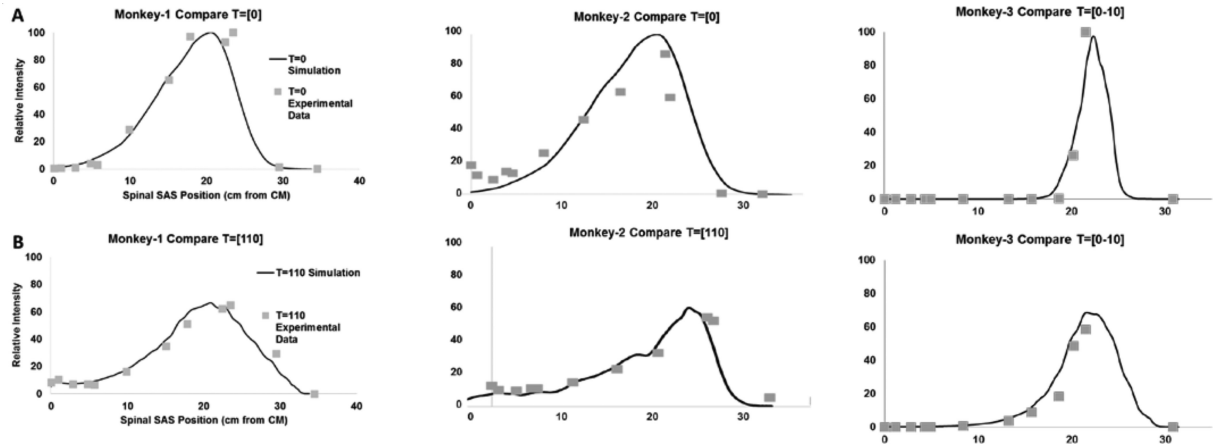

Fig. 6. Graphical front of the measured and simulated tracer concentration intensity along the neuraxis. Data plots compare the continuous simulation (black line) with the 12 planes of interest from the measured PET data, at (A) 10 minutes after infusion (T = 0 min), and (B) two hours after infusion (T = 110 min).

cranial and the spinal compartment due to pulsatile convection is zero. Accordingly, micro-mixing phenomena, not bulk flow, convey tracers from the injection site in caudocranial direction. Micro-mixing induces tracers dispersion from the injection site in caudocranial direction was demonstrated previously in human simulations with closed cranial and spinal CSF compartments [12], [22].

IV. Discussion

The paper presents a first of its kind study validating that IT administration with suitably chosen infusion settings can produce wide biodispersion of tracers along the neuraxis. Using in vivo MR and PET imaging, intrathecally administered tracers were tracked along the neuraxis over a period of two hours in three non-human primates (NHP). Imaging modalities were optimized to acquire two types of subject-specific information: (i) anatomical data to map animal geometry and CSF flow pulsations in the spinal subarachnoid space, as well as (ii) concentration measurements to track spatiotemporal tracer distribution profiles along the neuraxis. Moreover, we deployed a previously developed CFD method to predict the biodistribution of IT administered molecules by means of tracer dispersion experiments. The simulation results here confirm our prior work showing that inclusion of the hydraulic interaction between microanatomical features, CSF flow, and drug dispersion is significant to predict IT drug administration.

A computational procedure based on computational fluid mechanics principles for simulating tracer dispersion after IT administration in each of the monkey trials was presented. It followed an image processing and segmentation workflow previously introduced for humans [13] to accurately reconstruct individual anatomical features of the CSF filled-spaces in the entire cranial and spinal CNS. In addition, subject-specific CSF flow patterns that were observed inside the spinal subarachnoid spaces were recreated in the computer simulation by imposing deformable boundary conditions on the borders of the spinal CSF compartments. The precise magnitudes of the area deformations were determined from the subject-specific volumetric CSF flow data in three regions of interest located in the cervical, thoracic and lumbar spine. The precise area deformation along the neuraxis that cannot be directly observed with MRI was inferred from the observed amplitude attenuation of the CSF volumetric flow rates.

While our direct numerical simulations and prior ample bench testing on closed CNS models provide evidence in support of the hypothesis that micro-mixing phenomena convey tracers from the injection site in caudocranial direction, the spinal deformation and especially the exact determination of *location and extend of volumetric strain* still awaits validation by direct observation, which was not possible in our MRI study. We also did not attempt to create a biomechanical model of implicit fluid structure interaction between CSF and surrounding tissue compartments. Recent work by Sanchez and Lasheras [23], [24]. which were not available when this manuscript was first submitted, may be a step in this direction. Furthermore, the gradual attenuation of the stroke volume from cervical to thoracic and lumbar spinal region observed here is evidence in support of the deformation and geometry induced tracer transport hypothesis. Furthermore, our prior bench experiments clearly demonstrated that tracer transport mediated by pulsatile CSF needs no bulk convection; instead rapid biodistribution occurs due to geometry induced micro-mixing phenomena.

Simulated drug administration procedures were performed on computational domains that matched the individual animal's CSF-filled anatomical spaces, recreated their volumetric CSF flow oscillations, and emulated the IT administration settings including infusion catheter geometry and injection flowrates. *Without any further adjustable parameters*, tracer spread was predicted along the entire neuraxis for the duration of two hours in each monkey trial. Simulation of drug biodistribution is a significant improvement over traditional pharmacokinetic models which require a large number of adjustable kinetic parameters; and are thus prone to over-parameterization. Moreover, traditional pharmacokinetic models do not explicitly account for CSF anatomy, flow or infusion parameters, so that predic-

tion merely recreate observations for a single experimental run, but do not allow simulations with optimized IT parameters or subject-specific anatomy. The lack of sensitivity to key parameters in traditional pharmacokinetics methods was overcome in the present method. For the infusion settings in each animal specimen, the simulated spatiotemporal tracer concentration profiles closely matched the evolution and spatial extent of radiolabeled tracer spread observed in the experiments. The favorable agreement of both spatial as well as temporal profile data in each case supports the feasibility of the proposed computational approach for predicting the fate of IT administered tracer molecules.

The experiments demonstrated IT delivery as a viable administration route for targeting molecules to the spine or the brain confirming our earlier findings, which rested on extensive bench experiments on a human CNS surrogates [18], [22] and CFD predictions for human IT administration [14]. The in vivo experimental demonstration of wide tracer spread is significant, because earlier pioneering work by Bernards [11] drew unfavorable conclusions about the possibility of administering drugs by lumbar injection. In our monkey experiments, tracer reached the cervical region of the spine after only two hours. While we did not track tracers into the cerebral subarachnoid space, the experiments suggest that cerebral targets are reachable with IT administration. Our new finding establishes that wide dispersion with rapid ascent from the injection site towards the brain can be accomplished by suitable choices of IT infusion parameters. To achieve this highly desirable outcome, we selected higher infusion rates than Bernard's pig study. It should be mentioned that our tracers were biologically inactive thus preventing spinal tissue uptake which slows their spread, while Bernard's study deployed lipophilic drugs with substantial spinal tissue penetration.

The *geometry induced mixing theory* supported by computer predictions suggests that CSF pulsations inducing eddies around microanatomical features of the spinal CSF spaces serve as physical driving forces by which IT injected drugs are transported in the CSF. The implementation of in silico IT drug administration using existing CFD methods demonstrates our readiness to predict and optimize infusion methods for spinal or cerebral targets in individualized treatments.

We found that spatiotemporal drug profiles evolve in response to a canon of physicochemical factors including (i) infusion choices (infusion flow rate and impulse, catheter position), (ii) subject-specific CSF-mediated transport properties (size of anatomical spaces, CSF volumetric flowrate and frequency) and (iii) molecular and chemical kinetic properties of the injected species. Mathematical modeling provides quantitative guidelines for carefully selecting these factors for IT protocols that are optimal for a specific patient. Although uncertainties and interpatient variability are unavoidable in the medical practice, in silico design of administration parameters could assist physicians in determining IT therapy dosing strategies or inform research studies about the most efficient infusion protocols for delivering novel drugs. This predictive quality is especially important for novel drug leads, such as IT-administration of antisense oligonucleotides (ASO) to target the brain. In these cases, no prior clinical experience exists, and purely experimental findings from infusion studies in small animal models (rodents) routinely undertaken in today's preclinical trials are hard to scale for the human brain anatomy.

The NHP trials were structured to cover three distinct dispersion scenarios that are relevant for acute IT drug injection: (i) high infusion volume, fast infusion rate: monkey-1, (ii) high infusion volume, low infusion rate: monkey-2, and (iii) a low infusion volume, low infusion rate: monkey-3. The number of subjects was limited to three NPH specimen, because the aim was to validate subject-specific predictions. Accordingly, each individual experiment provided a whole spectrum of spatiotemporal data points with measurements distributed along the neuraxis and in time, which permitted quantitative comparison of tracer concentration profiles between simulations and experiment. Since the study was designed to validate predictions for a specific NHP subject, increasing the number of animals in the experimental cohort would not strengthen the predictive power for a subject-specific case, although we acknowledge that it would consolidate confidence of the method's routine use. In this tracer study we selected three animals, because the match between computations and experiments was satisfactory; additional trials would incur further unnecessary animal sacrifice.

A. Limitations

The current study addressed tracer dispersion for two hours relevant for acute IT drug applications. A future expansion could address chronic intrathecal drug delivery which would involve implantation of subcutaneous drug pumps which typically dose therapeutic agents at low flow rates for long periods of time (days, weeks, months). Our understanding derived from the CFD simulations [12]–[14], [19] suggests that chronic delivery strongly depends on molecular and chemical kinetic properties of the infused drugs. Long term studies would therefore need to account for specific drug uptake into tissue or special cell lines (lipophilicity and targeting specificity respectively), as well as half-life clearance by blood or excretory organs. Thus, biologically inert tracer imaging performed here would be suboptimal for long term studies. We also point out that infusion settings (bolus versus continuous infusion) and catheter geometry affect drug dispersion patterns via chronic infusion pumps. These additional aims are beyond the scope of this study.

Even though we deployed research imaging protocols superior to clinical imaging routines, the MRI scanner has limited resolution for acquiring data about the CNS anatomy and CSF flows. The proposed dura deformations could not be directly observed because the area displacements fall below the MRI imaging threshold. Therefore, our findings are based on inferred deformations whose exact magnitude and spatiotemporal distribution awaits experimental validation. In our monkey imaging, sub-millimeter voxel resolution permitted the reconstruction of large structures and some microanatomical structures especially nerve roots which are important for modeling geometry induced dispersion [13]. Unfortunately, smaller microanatomical features such as individual dorsal root fibers, arachnoid trabeculae, ligaments, spinal-arachnoid midline septa are below the MR image resolution threshold and were therefore excluded from the reconstruction. We also limited the CSF flow measurements

to three regions of interest in the cervical, thoracic and lumbar regions to avoid excessive scanning time for the animals. Another possible further expansion of this work could address the pulse related variations of tracer distribution among various CSF compartments as seen in recent MRI studies [25]. A recent review may provide the theoretical framework for such a study [26].

V. Conclusion

Using subject-specific simulations in three cynomolgus monkeys, we created new evidence supporting model-based predictions of tracer dispersion after IT injection without the need of adjustable parameters. The spatiotemporal distribution of the tracer was successfully predicted based on first principles using only anatomical information as well as CSF flow measurements that are available non-invasively. Simulations in monkey-3 were blind to tracer distribution experimental outcomes until the completion of the study. The predicted tracer distribution fell within 5% deviation of the measurements, which is within experimental error limits of PET imaging and MRI.

The experimental finding of wide tracer dispersion is significant, because it corrects the widely held belief that IT injection administers the drug only to a very narrow region close to the injection site.

We demonstrated CFD simulation of drug dispersion after acute IT infusion on massive scale covering the entire spinal CSF filled spaces. It demonstrates the feasibility of using image-based computational methods to predict tracer biodispersion throughout the entire central nervous system. The computational platform and multi-scale techniques shown for monkey in this study may serve as a practical tool to optimize infusion parameters for IT drug therapies such as gene or enzyme replacement therapy.

Computational methods that help assess and quantify the distribution of therapeutic agents to CNS tissues or sites of action are essential in the development and delivery of successful therapies to a wide range of critical neurological conditions. In silico experiments integrated with select animal validation could substantially shorten trial and error testing, and reduce the development time of novel dosing regimes or administration techniques.

Acknowledgment

The authors would like to thank the anonymous reviewers who provided feedback on the manuscript originally submitted to this journal on March 22, 2018, as well as the subsequent reviewers who assessed the resubmitted manuscript.

References

[1] R. D. Penn, "Intrathecal baclofen for spasticity of spinal origin: Seven years of experience," *J. Neurosurgery*, vol. 77, no. 2, pp. 236–240, Aug. 1992.

[2] G. Bennett *et al.*, "Evidence-based review of the literature on intrathecal delivery of pain medication," *J. Pain Symptom Manage.*, vol. 20, no. 2, pp. S12–S36, Aug. 2000.

[3] B. M. Bruel *et al.*, "Intrathecal drug delivery for control of pain," in *Treatment of Chronic Pain by Interventional Approaches: The American Academy of Pain Medicine Textbook on Patient Management*, T. R. Deer, M. S. Leong, A. Buvanendran, P. S. Kim, and S. J. Panchal, Eds. New York, NY, USA: Springer, 2015, pp. 433–444.

[4] J. Prager *et al.*, "Best practices for intrathecal drug delivery for pain," *Neuromodulation, Technol. Neural Interface*, vol. 17, no. 4, pp. 354–372, 2014.

[5] R. V. Duarte *et al.*, "Intrathecal drug delivery systems for the management of chronic non-cancer pain: Protocol for a systematic review of economic evaluations," *BMJ Open*, vol. 6, no. 7, Jul. 2016, Art. no. e012285.

[6] K. Gritsenko *et al.*, "*Drug selection for intrathecal drug delivery*," in *Atlas of Implantable Therapies for Pain Management*, T. R. Deer and J. E. Pope, Eds. New York, NY, USA: Springer, 2016, pp. 287–291.

[7] D. Wolf *et al.*, "The effect of bolus volume and mechanical forces on the biodistribution of ASOs following lumbar intrathecal administration in cynomolgus monkeys (S38.007)," *Neurology*, vol. 86, no. 16 Suppl., Apr. 2016, Art. no. S38.007.

[8] L. Howden *et al.*, "Three-dimensional cerebrospinal fluid flow within the human central nervous system," *Discrete Continuous Dynamical Syst.*, vol. 15, pp. 957–969, Mar. 2011. [Online]. Available: http://www.aimsciences.org/journals/displayArticlesnew.jsp?paperID=6042, Accessed: Jun. 20, 2019.

[9] A. Kuttler *et al.*, "Understanding pharmacokinetics using realistic computational models of fluid dynamics: biosimulation of drug distribution within the CSF space for intrathecal drugs," *J. Pharmacokinet Pharmacodyn*, vol. 37, no. 6, pp. 629–644, Dec. 2010.

[10] W. M. Pardridge, "The blood-brain barrier: Bottleneck in brain drug development," *NeuroRx*, vol. 2, no. 1, pp. 3–14, 2005.

[11] W. C. Ummenhofer *et al.*, "Comparative spinal distribution and clearance kinetics of intrathecally administered morphine, fentanyl, alfentanil, and sufentanil," *Anesthes*, vol. 92, no. 3, pp. 739–753, Mar. 2000.

[12] A. A. Linninger *et al.*, "Cerebrospinal fluid mechanics and its coupling to cerebrovascular dynamics," *Annu. Rev. Fluid Mechanics*, vol. 48, no. 1, pp. 219–257, 2016.

[13] K. M. Tangen *et al.*, "CNS wide simulation of flow resistance and drug transport due to spinal microanatomy," *J. Biomechanics*, vol. 48, no. 10, pp. 2144–2154, Jul. 2015.

[14] K. M. Tangen *et al.*, "Computational and In vitro experimental investigation of intrathecal drug distribution: Parametric study of the effect of injection volume, cerebrospinal fluid pulsatility, and drug uptake," *Anesthesia Analgesia*, vol. 124, pp. 1686–1696, May 2017.

[15] S. M. Hayek and M. C. Hanes, "Intrathecal therapy for chronic pain: Current trends and future needs," *Current Pain Headache Rep.*, vol. 18, no. 1, Dec. 2013, Art. no. 388.

[16] T. R. Deer *et al.*, "The polyanalgesic consensus conference (PACC): Recommendations for intrathecal drug delivery: Guidance for improving safety and mitigating risks," *Neuromodulation, Technol. Neural Interface*, vol. 20, no. 2, pp. 155–176, 2017.

[17] T. L. Yaksh *et al.*, "Current and future issues in the development of spinal agents for the management of pain," *Current Neuropharmacol.*, vol. 15, pp. 232–259, 2017.

[18] D. A. Wolf *et al.*, "Dynamic dual-isotope molecular imaging elucidates principles for optimizing intrathecal drug delivery," *JCI Insight*, vol. 1, no. 2, Jun. 2019, Art. no. e85311.

[19] Y. Hsu *et al.*, "The frequency and magnitude of cerebrospinal fluid pulsations influence intrathecal drug distribution: Key factors for interpatient variability," *Anesthesia Analgesia*, vol. 115, no. 2, pp. 386–394, Aug. 2012.

[20] H. D. M. Hettiarachchi *et al.*, "The effect of pulsatile flow on intrathecal drug delivery in the spinal canal," *Ann. Biomed. Eng.*, vol. 39, no. 10, pp. 2592–2602, Jul. 2011.

[21] H. W. Stockman, "Effect of anatomical fine structure on the flow of cerebrospinal fluid in the spinal subarachnoid space," *J. Biomech Eng.*, vol. 128, no. 1, pp. 106–114, Feb. 2006.

[22] K. Tangen *et al.*, "Clearance of subarachnoid hemorrhage from the cerebrospinal fluid in computational and in vitro models," *Ann Biomed. Eng.*, vol. 44, no. 12, pp. 3478–3494, Dec. 2016.

[23] A. L. Sánchez *et al.*, "On the bulk motion of the cerebrospinal fluid in the spinal canal," *J. Fluid Mechanics*, vol. 841, pp. 203–227, Apr. 2018.

[24] J. J. Lawrence *et al.*, "On the dispersion of a drug delivered intrathecally in the spinal canal," *J. Fluid Mechanics*, vol. 861, pp. 679–720, Feb. 2019.

[25] G. Ringstad *et al.*, "Brain-wide glymphatic enhancement and clearance in humans assessed with MRI," *JCI Insight*, vol. 3, no. 13, 2018, Art. no. 121537.

[26] S. B. Hladky and M. A. Barrand, "Mechanisms of fluid movement into, through and out of the brain: evaluation of the evidence," *Fluids Barriers CNS*, vol. 11, no. 1, Dec. 2014, Art. no. 26.